Manufacturability of AlSi10Mg overhang structures fabricated by laser powder bed fusion

Quanquan Han *, Heng Gu, Shwe Soe *, Rossi Setchi, Franck Lacan, Jacob Hill

Cardiff School of Engineering, Cardiff University, Cardiff CF24 3AA, UK

HIGHLIGHTS

- Fine base support enables distortion-free AlSi10Mg overhang structures manufactured by laser powder bed fusion.
- Part support needed to manufacture dross defect-free overhang structures when the nominal diameter is greater than 15 mm.
- Molten pools at dross zone found to be larger than that at the dross-free zone.
- Part support found to play a significant role in enhancing the compressive behaviour of full-circle overhang structures.

GRAPHICAL ABSTRACT
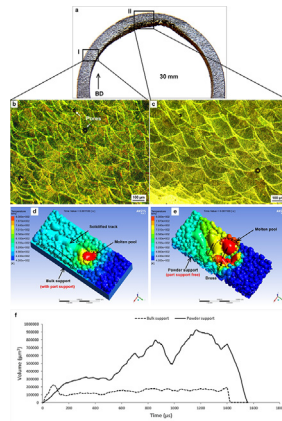
ABSTRACT

The main advantage of laser powder bed fusion (LPBF) is its use for directly manufacturing metal components with highly complex geometries. But the LPBF manufacture of overhang structures, also known as downward-facing surfaces, is a challenge because of the possibility of incurring distortion and dross defects. This paper presents a systematic examination of the manufacturability and structural integrity of AlSi10Mg overhang structures fabricated by LPBF using computational and experimental techniques. The experimental and simulation results indicate that the use of support structures facilitates the manufacturability and structural integrity of both full-circle and half-circle overhang structures. The influence of supports on circularity was found to be more beneficial as the diameter increased above 15 mm. The experiments also suggest that the use of supports plays a significant role in maintaining mechanical performance by successful fabrication of downward-facing surfaces free of dross defects. From a design perspective, small overhang features are preferable to large overhangs, especially when support removal is impractical. This study significantly contributes to design for metal additive manufacturing by providing an improved understanding of the manufacturability of overhang structures in applications intended for lightweight structural performance.

1. Introduction

Laser powder bed fusion (LPBF) is an additive manufacturing (AM) process that shows great potential in producing metallic parts with complex shapes [1,2]. A wide range of metallic materials have been

* Corresponding authors.
E-mail addresses: Hanq1@cardiff.ac.uk (Q. Han), Soes@cardiff.ac.uk (S. Soe).

successfully processed using LPBF in the past few years, including aluminium [3–5], titanium [6,7] and nickel [8–10] and these elements' alloys and composites. Several researchers have employed these materials to fabricate topologically optimised structures [11], auxetic structures [12] and cellular lattice structures [13]. But the manufacture of overhang structures – also referred to as downward-facing surfaces – is an enormous challenge when using the LPBF process because of the occurrence of distortion and dross defects. Distortion is primarily caused by residual thermal stress induced by rapid solidification [14]. In contrast to self-supported geometries, which benefit from being anchored to the layer below, overhang geometries lack support and can easily become distorted during the building process. Dross defects in LPBF are generally thought to be induced by the absorbed energy input, which is much higher at the powder-supported zone compared to the solid-supported zone; this situation further gives rise to the difference in molten pool size at the two zones [15].

In order to eliminate distortion and dross defects, external support structures are required to support the overhang geometries during the LPBF process [16–18]. The use of support structures, however, results in several drawbacks, such as increased manufacture time and complex post-processing. Previous studies have focussed on the geometrical design and optimisation of the support structures to address these problems. For instance, Calignano [15] employed the Taguchi robust design method to optimise the self-supporting overhang structures in aluminium and titanium alloys fabricated by LPBF. Her experimental results indicated that the downward-sloping faces could be manufactured without supports at angles of up to 30°, although not without detrimental effects on surface roughness. The author found that the quality of the overhang geometries could be improved using optimised supports and part orientation in the LPBF machinery. Strano et al. [19] proposed a novel approach for the design and optimisation of cellular support structures in additive manufacturing. Their implicit function approach enables geometries to be designed by mathematical expressions, which means that different cellular structures may be easily defined and optimised to achieve graded structures processed by LPBF. More recently, Langelaar [20] proposed a combined approach that enables the simultaneous optimisation of part geometry and supports layout and build direction based on 2D test problems, which allows designers to determine a suitable strategy to balance manufacturing costs and part performance. Mezzadri et al. [21] investigated the topology optimisation of self-supporting structures for additive manufacturing. Their study defined (1) the design domain where the topology was conducted, (2) the loading and boundary conditions and (3) the cost function in order to formulate the generation of support structures as a topology-optimisation problem.

A few studies have investigated the effects of support structures on overhang parts manufactured by LPBF. For example, Kajima et al. [22] studied the effect on fatigue strength from adding support structures to Co-Cr-Mo alloy overhang geometries. The authors found that the supported specimens had more than twice the fatigue strength than the unsupported specimens, which they explained by the reduction in residual strain that prevented the formation of microcracks led by thermal distortion in the supporting parts. Wang et al. [23], who investigated the effects of both thin-wall tooth contact and solid-gap support structures on Ti6Al4V overhang structures fabricated by LPBF, found that the tooth-contact parts exhibited lower Vickers hardness values compared to the solid-gap parts. This occurred because the solid part under the solid gap acted as a heat sink and enhanced heat dissipation during the manufacturing process. Sing et al. [24] adopted a statistical approach to investigate the manufacturability and mechanical behaviour of LPBF manufactured lattice structures. The authors found that the accuracy was most sensitive to laser power compared to layer thickness and scanning speed. Calignano [25] investigated the accuracy and roughness in the LPBF of AlSi10Mg alloy; it has been found that the surface roughness is mainly caused by the process parameters, orientation and position of the part with respect to the recoating blade, and by the presence of partially fused particles that adhere to the molten part.

From an AM design perspective, avoiding overhang configurations is impractical when redefining existing designs or creating new structures. In both cases, the goal is to achieve lightweight performance while facilitating strength, stiffness and other functional needs. In the present study, a circular structure was selected as a basis to understand the effect of support structures on manufacturability and structural integrity. The underlying principle is that circular shapes are commonly employed in the creation of shafts and holes in engines and other mechanical devices, and the dimensional stability and mechanical performance of AM parts are both critical while the parts are being integrated with standard components [26]. For bulky machined components, the integration of circular shapes (e.g. holes) is attractive from a weight perspective because of the minimum possibility of stress concentration under externally applied loads [27]. In other cases, the use of conformal circular channels has been demonstrated to provide improved cooling efficiency in injection mould tooling and other heat-sink applications [28]. In general, circular configurations show less inertial sensitivity under impact, which enables the creation of unique circular cellular lattice structures for energy-absorption applications [29]. Similar design rules for circular structures may be implemented in the further development of topology-optimisation methods, thus enhancing these structures' capabilities for AM design optimisation [30].

The studies noted above have indicated that overhang structures are currently limited to either manufacturability or structural performance, although none have considered both factors concurrently. The aim of the present study was thus to evaluate the manufacturability of circular structures, in particular by assessing their corresponding mechanical performance characteristics. A combination of experimental and computational techniques was employed to obtain a better understanding of the issues associated with overhang structures, thereby providing practical insights into designing for additive manufacturing. By extension, the methodologies implemented in the present study should lay the foundation for characterising new shapes, materials and process parameters to achieve optimum AM design solutions.

2. Experimental and simulation methods

2.1. Materials and LPBF process

The material used to fabricate the overhang structures in this study was AlSi10Mg alloy, acquired from Renishaw (Gloucestershire, UK), with an average particle size of 43 μm. A Renishaw AM250 system (Gloucestershire, UK) with a modulated ytterbium fibre laser with a wavelength of 1071 nm was used to manufacture the overhang samples under optimum manufacturer process conditions (laser power 200 W, hatch spacing 130 μm, powder layer thickness 25 μm and laser scanning speed 500 mm/s). These main process parameters were optimised via measuring the relative density of the as-fabricated cubic samples (10x10x10 mm), which was found to be greater than 99.9%. A 'chessboard' scanning strategy was employed, with the rotation angle between each adjacent layer set to 67° to eliminate the chance of scan lines repeating themselves directly on top of one another, thus leading to poor bonding and material properties.

2.2. Overhang shapes and support

The overhang structures used in this study included both full-circle and half-circle structures with a nominal diameter (inner diameter) varying from 5 to 30 mm and a fixed wall thickness of 5 mm. Renishaw QuantAM build-preparation software was used to generate the support structures. In this study 'part support' and 'base support' are defined as structures that provide support for the inner circle and the part base, respectively. Both medium and fine supports were employed to build the overhang structures in order to study the influence of support on build quality (e.g. distortion, surface roughness and mechanical properties).

Table 1
Parameters for fine and medium base supports.

Parameter	Value	
Support type	Fine	Medium
Cross-section	Circle	Circle
Diameter	0.4 mm	1.25 mm
Cap diameter	0.2 mm	0.5 mm
Cap height	0.2 mm	1 mm
Conical angle	85°	70°
Cluster spacing	0.5 mm	1.5 mm
Support spacing	0.5 mm	1 mm
Support count	5	5

Table 1 and Fig. 1 show the parameters for the fine and medium base supports used in the study. The primary difference between the two types of support is that fine base support offers more contact areas compared to medium support.

2.3. Computational techniques

2.3.1. Macroscale LPBF modelling

Recent advancements in LPBF simulations have enabled the prediction of geometric warpage, which has helped in developing compensated geometries to achieve components with improved accuracy [31,32]. Simufact Additive (henceforth 'Simufact'), which was used in this study, identifies problems with distortion and residual stresses based on macroscale modelling analysis. In this setup, inherent strains (produced in the building process by thermal strains, plastic strains and phase transformation) are calibrated from experimentation, such as by measuring the distortion after cutting the distorted cantilever beam and then running simulations to match the experimental values. This method, which uses voxel-element generation and layer-wise scanning, offers much faster computation time than either the mesoscale or microscale modelling approaches, which use layer-wise scanning with detailed thermomechanical data or move the heat source using fully transient thermomechanical coupling. In this study, both full-circle and half-circle displacement models (with and without support) were simulated based on the inherent strain values (Ex = −0.008, Ey = −0.003, Ez = −0.03) estimated for AlSi10Mg alloy, with the processing parameters corresponding to an LPBF machine fitted with 200 W laser power.

2.3.2. Microscale LPBF modelling

Because Simufact does not support microscale modelling, ANSYS Fluent was employed to model a moving laser beam in order to analyse the changing behaviour of the molten pool with respect to the interaction with solid and powder boundary layers. The modelling geometry was limited to a rectangle representing a few layers of an overhang region. The discrete element method (DEM) and MATLAB were first employed to realise the initialisation of the randomly distributed powder in this simulation. The three-dimensional mass, momentum and energy-conservation equations are as follows [33,34]:

$$\frac{\partial \rho}{\partial t} + \nabla \cdot \left(\rho \vec{v} \right) = \frac{\partial \rho}{\partial t} + \frac{\partial (\rho u)}{\partial x} + \frac{\partial (\rho v)}{\partial y} + \frac{\partial (\rho w)}{\partial z} \tag{1}$$

$$\frac{\partial}{\partial t} \left(\rho \vec{v} \right) + \nabla \cdot \left(\rho \vec{v} \vec{v} \right) = -\nabla p + \nabla \cdot (\tau) + \rho \vec{g} + \vec{F_f} \tag{2}$$

$$\frac{\partial (\rho H)}{\partial t} + \nabla \cdot \left(\rho \vec{v} H \right) = \nabla \cdot (k \nabla T) + S_h \tag{3}$$

where ρ is material density, t is time, u, v and w are the component velocities in the x, y and z directions (respectively) of resultant velocity $\vec{v}$, p is static pressure, τ is the stress tensor due to the viscous stress on the element surface as a result of viscosity, $\rho \vec{g}$ and $\vec{F_f}$ are gravitational body forces and external body forces (respectively), H is enthalpy, k is thermal conductivity and S_h is a volumetric heat source.

The fluid in this model was assumed to be Newtonian and with laminar flow; the enthalpy-porosity technique [35] was applied to simulate the melting and solidification processes. For the external boundaries of the calculation domain, thermal conduction, convection and radiation were applied on the side and bottom surfaces of the substrate. The energy-balance equation is expressed as:

$$k \cdot \frac{\partial T}{\partial \boldsymbol{n}} = -h_c(T - T_{env}) - \sigma \varepsilon \left(T^4 - T_{env}^4 \right) \tag{4}$$

where h_c is the heat convection coefficient, σ is the Boltzmann constant, ε is radiation emissivity and T_{env} is the environmental temperature.

Two phases were considered in this study so that the time-variant interface between gas and substrate could be tracked; this interface moved according to the melting and fluid flow condition inside the molten pool. The volume of fluid [36] method was employed to capture the free surface between the gas and AlSi10Mg phases. The volume fraction was updated during every time step to track the liquid-gas free surface, while mass, momentum and energy sources were added to this
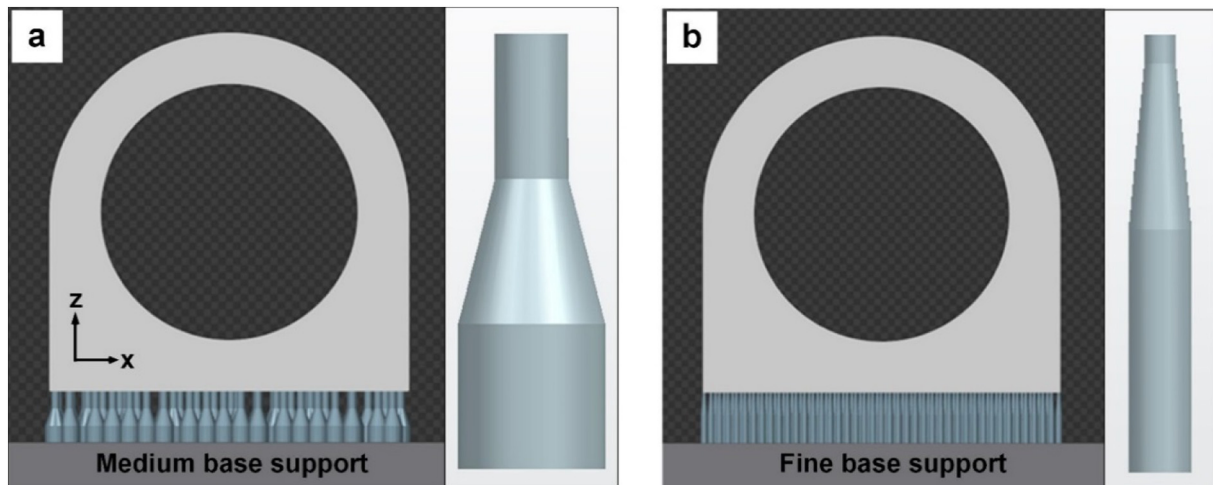
Fig. 1. Full-circle overhang structure with (a) medium and (b) fine base support.
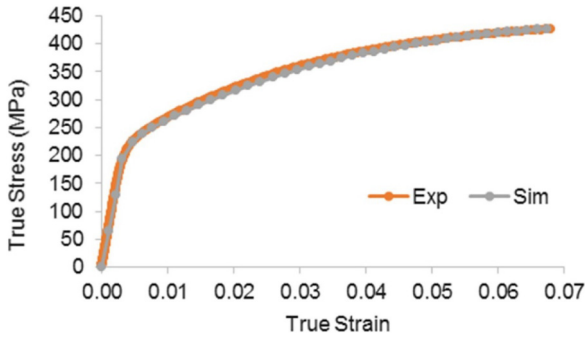
Fig. 2. Experimental and simulated true stress and true strain curves of the tensile parts.

interfacial boundary. The conservation equation for the volume fraction may be expressed as [37]:

$$\frac{\partial F}{\partial t} + \nabla \cdot \left(\overrightarrow{v} F \right) = 0 \tag{5}$$

where F is denoted as the volume fraction of a certain phase.

A Gaussian-distributed laser beam was applied to simulate the heat source on the free surface between the gas and metal phases. Assuming that elements with a total number of n are located on the interface within the effective laser beam range, the volumetric heat source S_h may be expressed as:

$$S_h = \frac{P_{laser} * \eta}{V_{cell} * \int_1^n \exp\left(-\frac{3 * r_n^2}{r^2} \right)} * \exp\left(-\frac{3 * r_n^2}{r^2} \right) \tag{6}$$

where V_{cell} is the element volume, P_{laser} is laser power, η is laser power efficiency and r_n is the radial distance from the laser beam centre.

Two surface-tension forces were included in this model: (1) surface-tension force f_{sn} normal to the free surface generated as a result of the curvature developed by the interface between the AlSi10Mg and gas phases and (2) the Marangoni shear force f_{st} tangential to the free surface generated as a result of surface-tension difference attributed to the temperature difference within the molten pool surface. The surface-tension forces may be defined as [38]:

$$f_S = f_{sn} + f_{st} = \sigma \cdot \kappa \cdot \overrightarrow{n} + \nabla_t \sigma \tag{7}$$

where σ is surface tension, κ is surface curvature and $\overrightarrow{n}$ is the vector normal to the surface.

2.3.3. Structural analysis

Abaqus was employed for surface-to-surface contact analysis using an 8-mm-diameter pin pressed directly against the apex of the geometry until failure occurred. In this setup, we created a 2D plane-stress model for the part and a discrete rigid wire model for the pin, respectively. Tangential behaviour with a frictional coefficient of 0.2 and hard-contact nominal behaviour were assigned for the contact interactions. The elastoplastic material properties (modulus of elasticity = 63 GPa, yield strength = 200 MPa and ultimate tensile strength = 425 MPa at 6.5% strain) used for simulation were extracted and calibrated from the tensile testing of as-fabricated AlSi10Mg specimens produced by LPBF. The dataset was found to be comparable to that available in the material data assessed in previous work [39]. The following procedures detail the elastoplastic material modelling and calibration steps followed in Abaqus.

(1) After examining the experimental data (Fig. 2), the initial straight portion of the stress-strain curve was translated into the modulus of elasticity (63 GPa).
(2) The end point of the straight line before the shoulder portion was taken as the yield point, which was equal to 200 MPa. (Note that the 0.2% offset provided a higher value of 234 MPa, but the simulated curve did not fit well using this point.)
(3) All the experimental stress-strain data points were then converted into true stress σ_{true} and true strain ε_{true} data using the following equations:

$$\sigma_{true} = \sigma_{engineering} * \left(1 + \varepsilon_{engineering} \right) \tag{8}$$

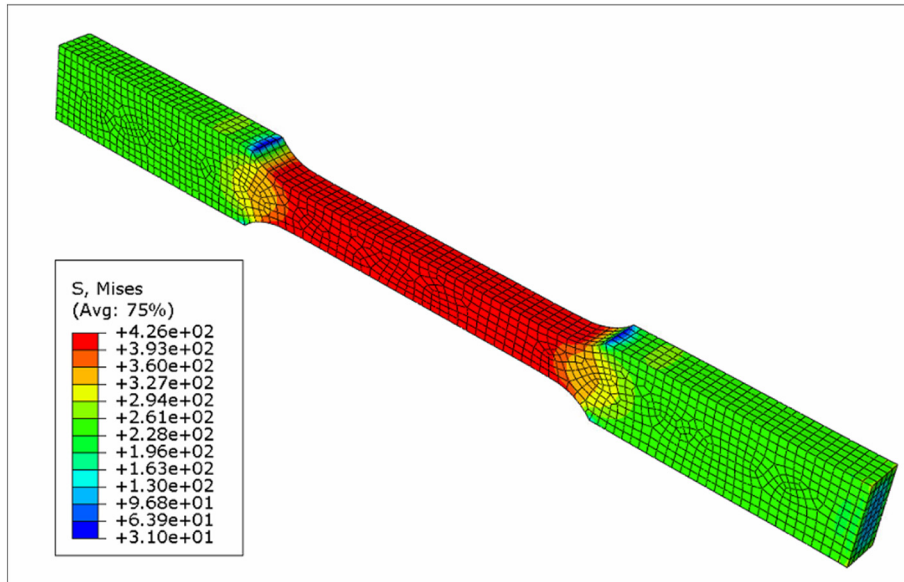$$\varepsilon_{true} = \ln \left(1 + \varepsilon_{engineering} \right) \tag{9}$$

Fig. 3. Illustration of the Von Mises stress distribution of the tensile model at 6.5% strain.

(4) After the removal of the elastic strain portion, the remaining data was applied as yield-stress (starting with 200 MPa) and corresponding plasticity-strain values.

(5) The tensile model was then meshed using an element type of C3D20R (a 20-node quadratic brick with reduced integration) with an approximate global element size of 1 mm (Fig. 3).

(6) In the simulation, one end of the model was fully fixed, while the other was displaced for 3 mm (equal to approximately 7% strain), which allowed the extraction of the true stress and strain data from the node that showed the maximum values.

(7) The simulation output data ('Sim' in Fig. 2) was then overlaid on top of the experimental input data ('Exp' in the figure). The simulated data was validated as being well matched in the calibration process for use in further finite element analysis.

In the simulation, the pin was allowed to move downward vertically and quasi-statically, while the base of the geometry was fully fixed. Applying the CPS4R element type (a 4-node bilinear plane stress quadrilateral

with reduced integration and hourglass control), the geometry was then meshed with 0.25 mm approximate global size control. The force and displacement of the pin were captured from the pin's centre within the simulation; the stress and strain distribution of the model were then analysed.

2.4. Characterisation techniques

In order to examine the surface finish at different build positions, a Taylor Hobson surface finish tester was used to measure the roughness of the inner surface under 0.5 mm/s measuring speed. A Mitutoyo Euro Apex coordinate measuring machine (CMM), with a Renishaw REVO-1 five-axis tactile probe, was employed to examine the circularity of both the inner and outer circle profiles in the full-circle overhang structures and to study the influence of supports on geometrical accuracy and structural integrity. A ZwickRoell compression tester was used to perform the compression testing (with a strain rate of 2 mm/min) on both full-circle and half-circle overhang structures at room temperature. Optical microscopy (OM) and scanning electron microscopy
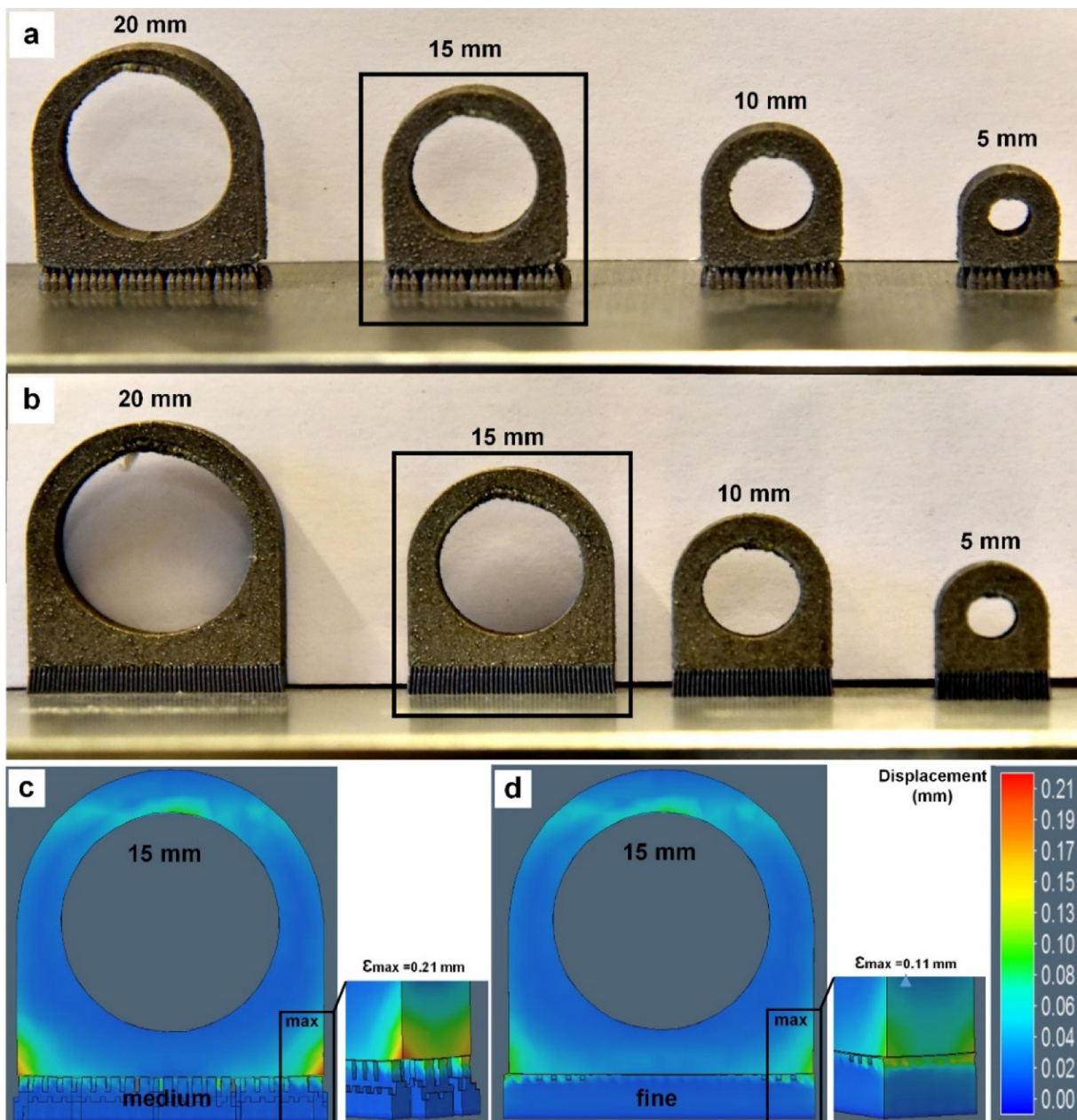

Fig. 4. As-fabricated full-circle overhang structures with (a) medium base support and (b) fine base support; (c) simulation results of the 15 mm full-circle structures.
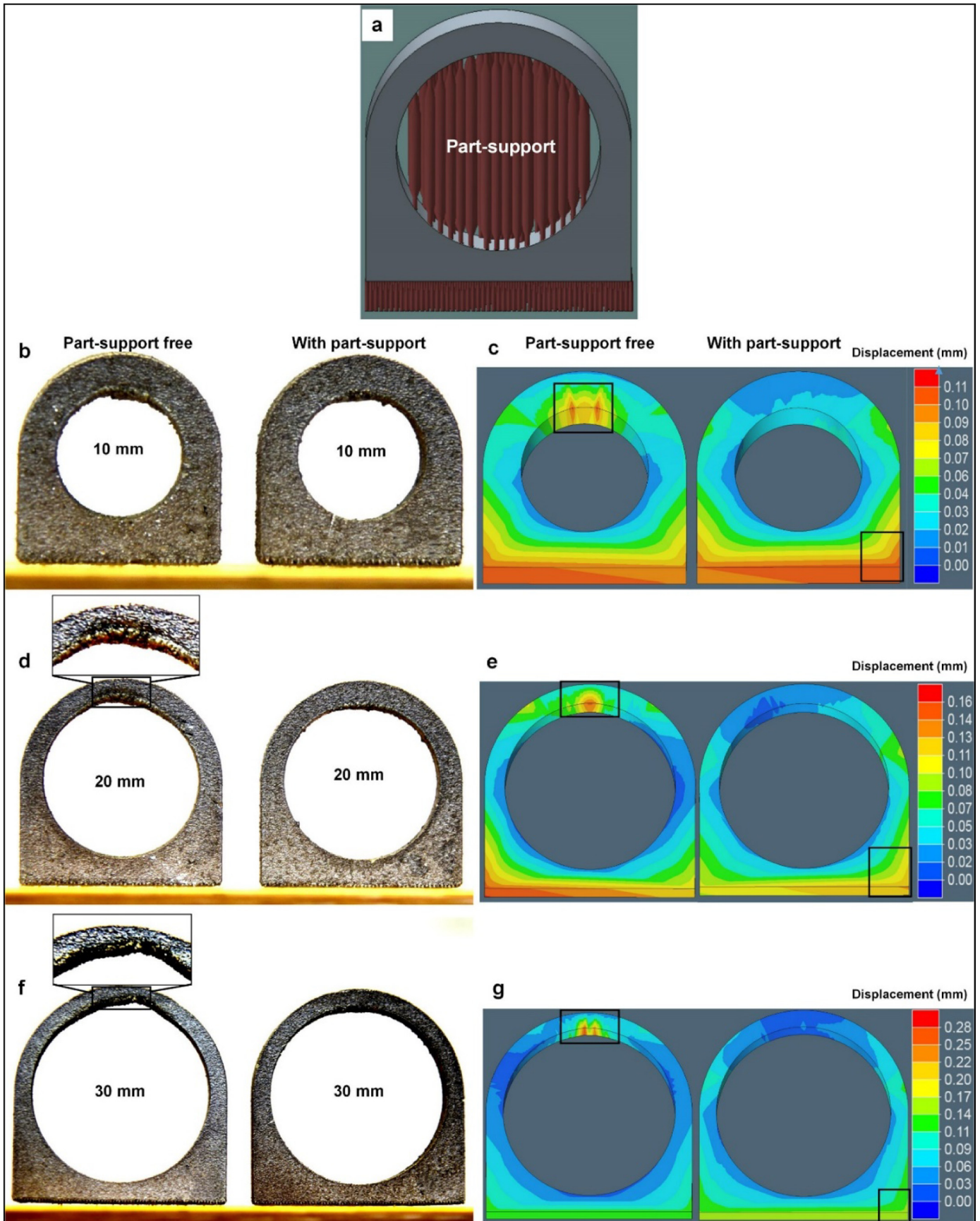
Fig. 5. The fabricated full-circle overhang structures and corresponding simulations.

(SEM) were used to inspect the molten pool and fracture surfaces. Prior to the OM inspection, the samples were etched using Keller's reagent for 20 s (190 ml distilled water, 5 ml HNO$_3$, 3 ml HCl, 2 ml HF).

3. Results and discussion

3.1. The effect of base support

Fig. 4 shows the as-fabricated full-circle overhang structures with medium and fine base support, respectively. Distortion, which was noticeable for all parts built with medium base-support structures, increased noticeably as the nominal diameter increased from 5 to 20 mm (Fig. 4a). In contrast, the full-circle structures built with fine base support (shown in Fig. 4b) were distortion defect–free, even when the nominal diameter was increased to 30 mm (not shown in Fig. 4b).

Fig. 4c and d show the simulation results for total displacement when the base support was changed from medium to fine; these simulation results were then useful for further understanding of the distortion mechanism involved. The maximum distortion sites for both overhang structures were found to be at the contact corners between the base support and the overhang specimens. The maximum displacement values calculated in Simufact for the 15-mm-diameter specimen (0.21 mm for medium base support and 0.11 mm for fine base support) were validated by our samples. One possible explanation for this situation could be that the fine base support offered more contact areas between the support and overhang specimens compared to the medium base support. This finer support promoted heat transfer from specimens to the underlying plate; the residual thermal stress and distortion were thus significantly reduced. Indeed, the cap diameter of the fine base support was 0.2 mm, compared to 0.5 mm for the medium base support (Table 1).

Due to the significant displacement difference between the two types of support (and the resulting influence on build quality), fine base support specimens were used for the remainder of this study to
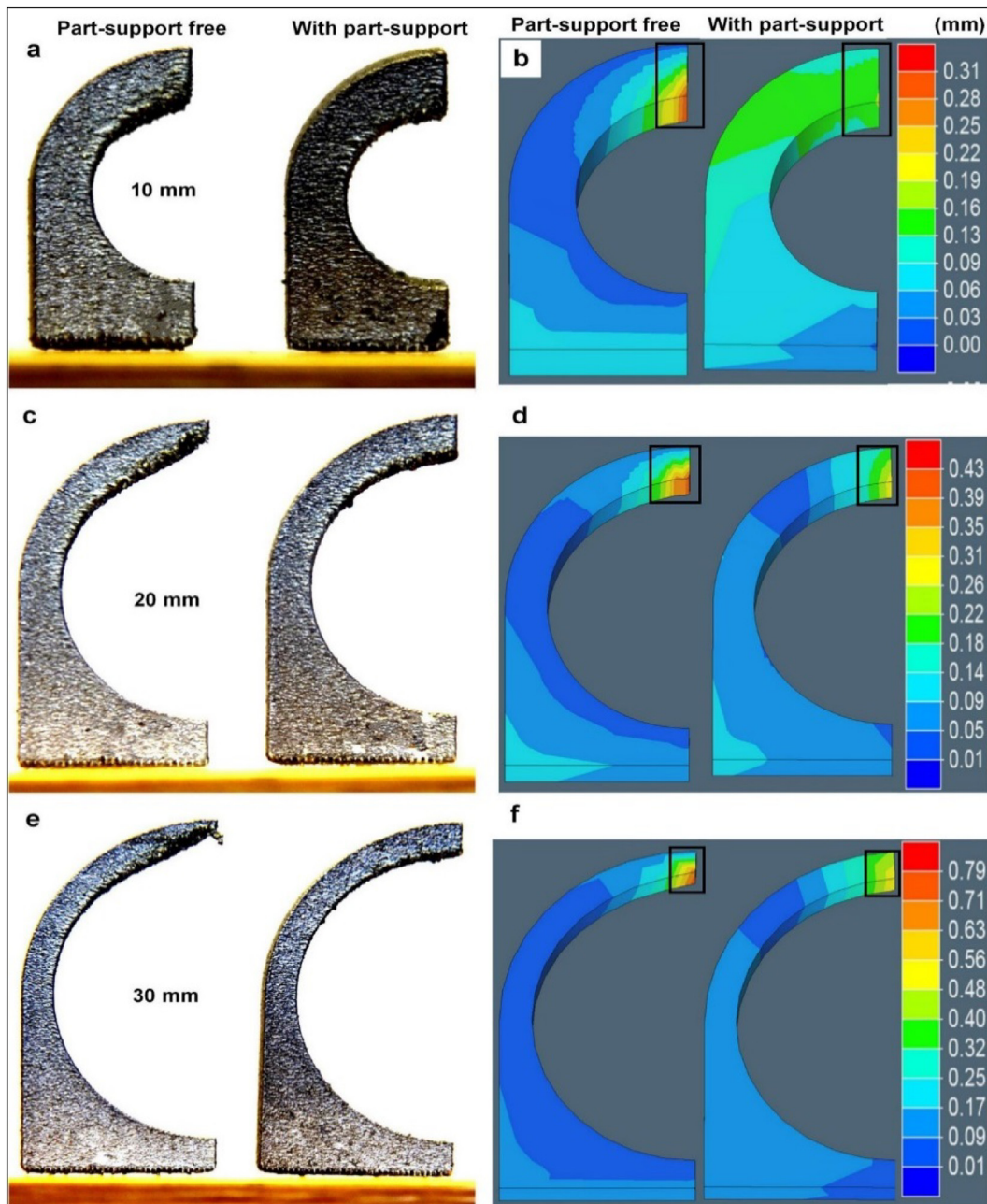

Fig. 6. The fabricated half-circle overhang structures and corresponding simulations.

build both full-circle and half-circle overhang structures in order to investigate the effects of part support on manufacturability, microstructure and mechanical performance.

3.2. The effect of part support

Fig. 5 shows the fabricated full-circle overhang structures and the corresponding simulation results of displacement when the nominal diameter was increased from 10 to 30 mm. The overhang structures were built under 'part-support free' and 'with part support' conditions (henceforth PSF and WPS, respectively) in order to investigate the effect of part support on distortion and dross defects. Part support was generated by QuantAM software and manually removed prior to further analysis (Fig. 5b, d and f); the part support was built inside the inner circle to support the overhang structure along the build direction (Fig. 5a).

As the figure shows, with an increase in nominal diameter from 10 to 30 mm, the dross defect tended to be more pronounced in the PSF samples, while the WPS samples were not affected to the same degree. This implies that part support enhanced the manufacturability of the full-circle overhang structures, particularly the downward-sloping faces. In general, due to the high thermal stress accumulation that occurs when using the LPBF process, downward-sloping faces with angles smaller than 45° (the angle between the X-Y plane and the face) must be supported by part support [15]. The literature has established that for angles greater than 45°, a unique self-supporting condition enables a new layer to be supported by a layer underneath [40,41]. In our study, the downward-sloping faces in full-circle overhang structures increased with an increase in nominal diameter from 5 to 30 mm, which led to further accumulation in the residual stress and displacement (and thus the occurrence of dross defects). The part support created in our study managed to hold the overhang structure, particularly the areas with an angle smaller than 45°. No dross defect occurred as a result.

Fig. 5c, e and g show the simulated total displacement of the full-circle overhang structures after the removal of both base support and inner-circle support. When the nominal diameter was 10 mm, the displacement was found to be 0.11 and 0.1 mm for PSF and WPS samples, respectively, while the values increased to 0.28 and 0.11 mm when the nominal diameter increased to 30 mm, which was in agreement with the experimental findings. We should note that for the PSF structures, the maximum displacement was found to take place at the top-downward sites (indicated in the figures) where the face angle was 0°. The displacement in the WPS samples, in contrast, was found to be less affected by an increase in nominal diameter, which was around 0.1 mm. The maximum displacement occurred at the edge site between base support and overhang structures (indicated in the figures), where the stress concentration took place. After the removal of the base

support, the accumulated residual stress was released, which caused the overhang structures to become distorted at the edge sites.

Fig. 6 shows the fabricated half-circle overhang structures and the corresponding simulation results of displacement when the nominal diameter was increased from 10 to 30 mm. Compared to the full-circle structures, the part support we employed seemed to be more influential among the half-circle overhang structures. The simulation results indicated that for the half-circle overhang structures, the maximum displacement under both conditions (PSF and WPS) took place at the top-downward sites (indicated in Fig. 6b, d and f). The displacement values for the PSF structures were larger than those of the WPS structures when the nominal diameter was fixed.

Fig. 7 shows the simulated total displacement of full-circle and half-circle overhang structures under both the WPS and PSF conditions. For full-circle structures, the effect of part support was found to be more influential when the nominal diameter was larger than 15 mm. This situation, which was in agreement with the experimental findings, suggested that the maximum nominal diameter would be 15 mm when the LPBF process was used to manufacture the PSF overhang structures. Compared to full-circle overhang structures, the part support was more influential among the half-circle structures. The simulated total displacement was almost linearly proportional to the nominal diameter. We should note that the maximum displacement for the 'half-circle with part support' (HCWPS) structures occurred at the top-downward sites rather than the interaction edge sites, which was where the 'full-circle with part support' (FCWPS) overhang structures exhibited the maximum displacement. This situation occurred because the full-circle structure offered larger contact areas at the top sites, which enabled the dispersion of heat energy to the two symmetrical directions, thus reducing residual thermal stress.

3.3. Surface roughness and circularity

Fig. 8 shows the measured roughness of the 'full-circle part-support free' (FCPSF) overhang structure (30 mm nominal diameter) at different positions; five different regions (I-V) were measured on the left half of the structure. The face angle at region III was 90°, where the measured roughness indicator R_a was ~5.9 μm. The roughness was not found to vary much when the face angle was greater than 90°; the R_a values were determined to be 1.75 and 1.42 μm at regions I and II, respectively. The roughness exhibited a significant increase, however, when the face angle was less than 90° at regions IV and V; the R_a values were then 29.3 and 41.6 μm, respectively. The surface roughness was found to increase with a decrease in the face angle due to the impact of the staircase effect. This effect is generally associated with the formation of dross defects, which can lead to increased surface roughness.
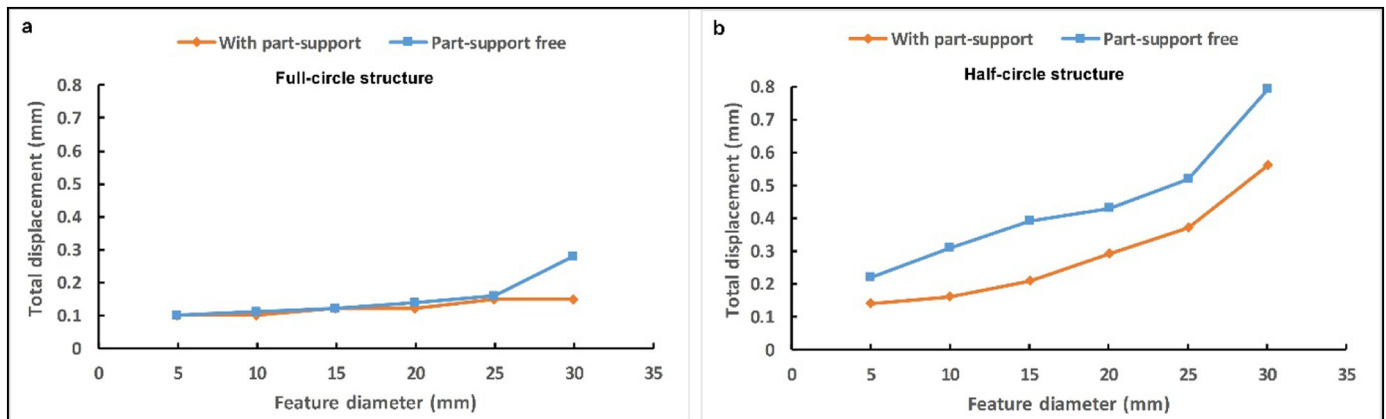

Fig. 7. The simulated total displacement of (a) full-circle and (b) half-circle overhang structures under both 'with part support' (WPS) and 'part-support free' (PSF) conditions.
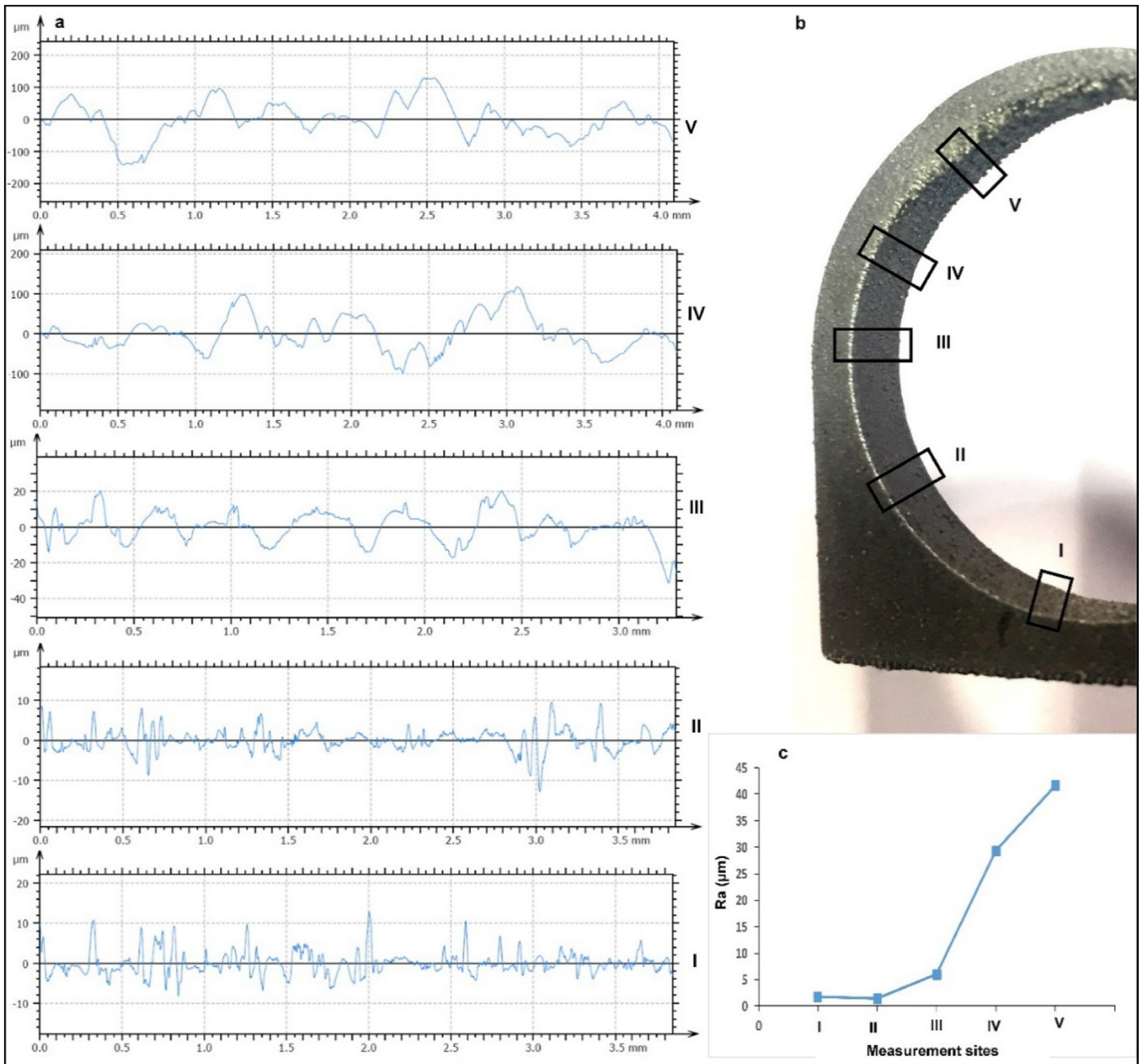
Fig. 8. The measured roughness of the 'full-circle part-support free' (FCPSF) overhang structure at different positions.

Fig. 9 shows the CMM-scanned coordinates of the 30 mm full-circle overhang structure relative to the machine origin under both PSF and WPS conditions. Both the inner and outer profiles were measured. Because the outer profile had a half-circle shape, the circularity of the outer profile was determined based on the measurement of the half-circle profile. The radius of the CMM probe was 1.5 mm. The coordinates that were captured were located at the probe centre, which means that the profile we obtained was offset from the original overhang structure profile by the probe radius (1.5 mm). In general, a smaller circularity value corresponds to a more spherical geometry profile. When the nominal diameter was fixed at 30 mm, the inner and outer circularity values obtained for the PSF part were 0.74 and 0.11, respectively, while the values were measured at 0.22 and 0.12 for the WPS structure. Little difference in outer profile circularity was found when the part was fabricated under either condition, while inner-profile circularity exhibited a significant difference. The increase in circularity from 0.22 to 0.74

implies that part support contributes to overhang structure manufacturability and structural integrity by minimising the formation of dross defects. We should note that the surface roughness and measured circularity value of 0.22 shown in Fig. 9b might depend on the manual removal of the inner-circle supports.

The CMM-obtained circularity values of the full-circle overhang structures for both the inner and outer profiles shown in Fig. 10 were then useful for further analysis of the part supports' influence on the overhang structures' manufacturability. Due to the CMM probe's size limitation (1.5 mm radius), the inner circularity values of the overhang structures with 5 mm nominal diameter were not measured. Both the PSF and WPS structures exhibited a consistent outer circularity: the determined value was around 0.1 when the nominal diameter was increased from 5 to 30 mm. Part support exhibited a more significant effect on inner circularity: for the WPS structures, the circularity value was found to be ~0.15 when the nominal diameter was increased
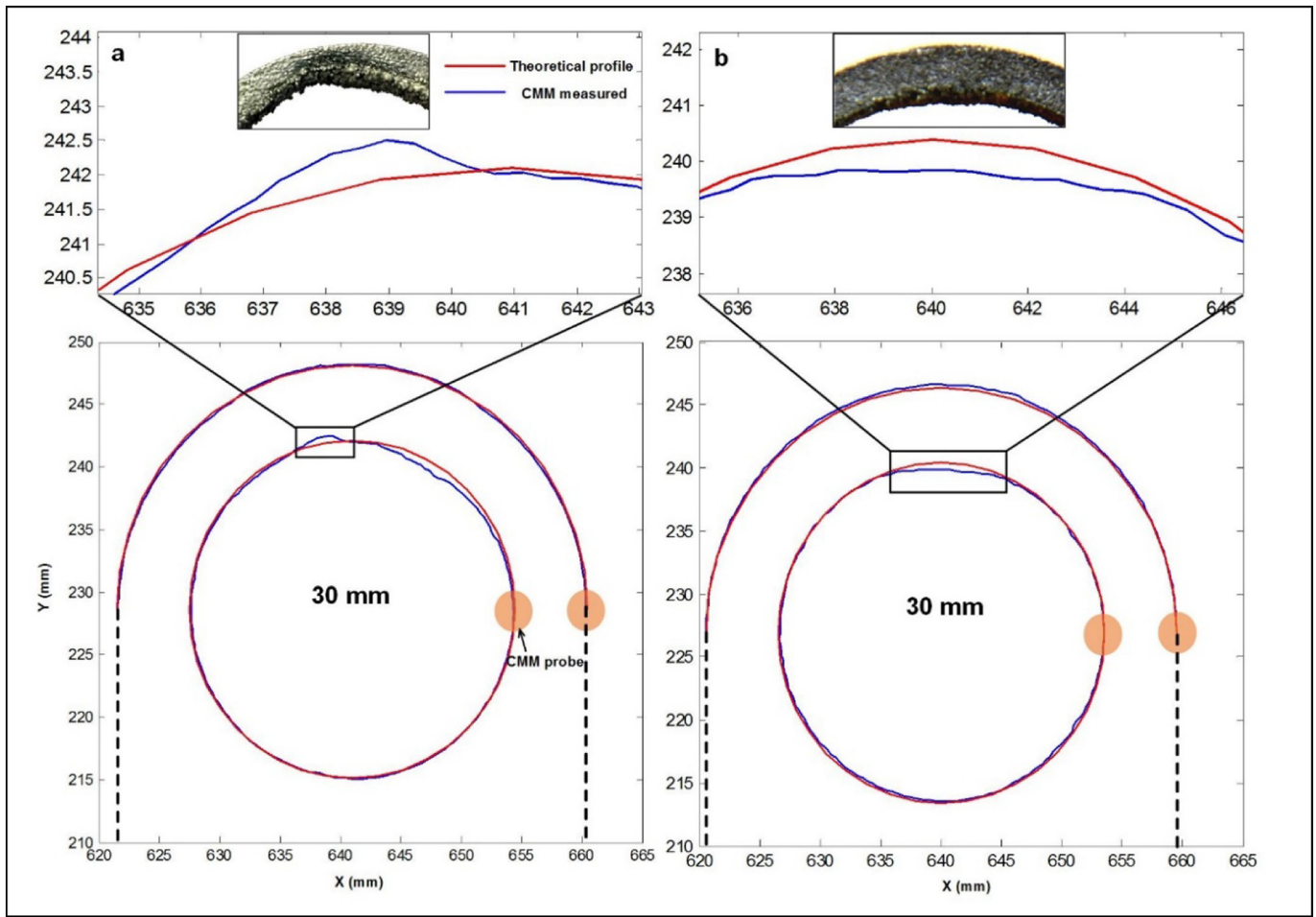
Fig. 9. The CMM-scanned X-Y coordinates of the 30 mm full-circle structure relative to the machine origin under (a) PSF and (b) WPS conditions.

from 10 to 30 mm, while the circularity increased dramatically when the nominal diameter was increased from 15 to 30 mm. When the nominal diameter was smaller than 15 mm, the average circularity value was ~0.17, while this value increased to 0.65 when the nominal diameter was greater than 15 mm.

The 25 mm structure exhibited a slightly larger circularity value of 0.91 compared to the 30 mm structure (0.74), which could be explained by measurement uncertainties and/or a difference in surface finish between the components. This finding implies that part support is generally needed to manufacture dross defect–free overhang structures when

the nominal diameter is greater than 15 mm. We should note that the surface roughness of both inner and outer structures could significantly affect the results from a tactile probe; the circularity values we measured thus were a coupled result of surface roughness and the type of part support we used.

3.4. Microstructure and mechanical behaviour

Fig. 11 shows the molten pools at two different positions on the FCPSF overhang structure. The microstructure at regions I and II
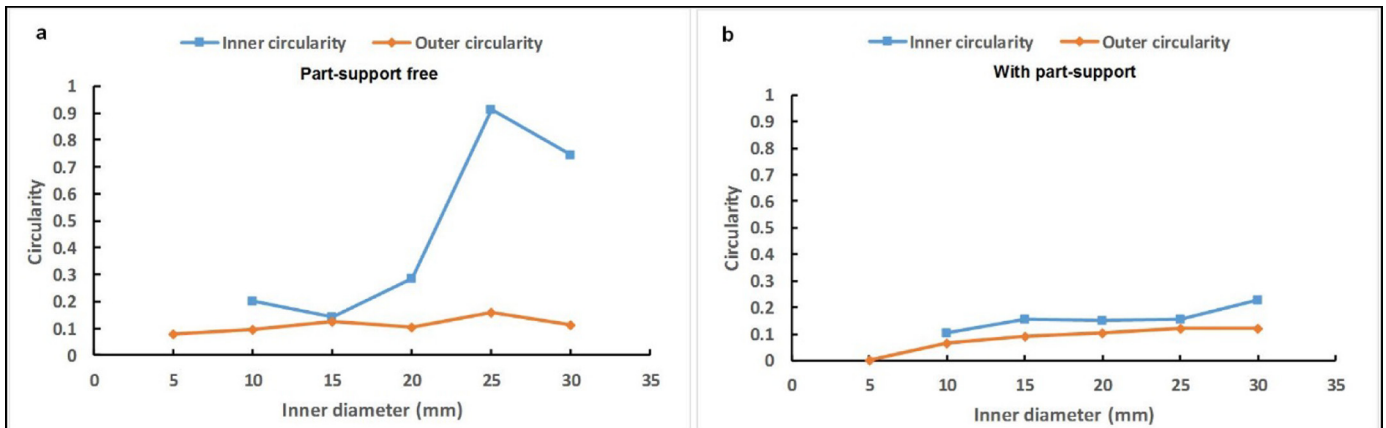

Fig. 10. The measured circularity of full-circle overhang structures: (a) PSF and (b) WPS.
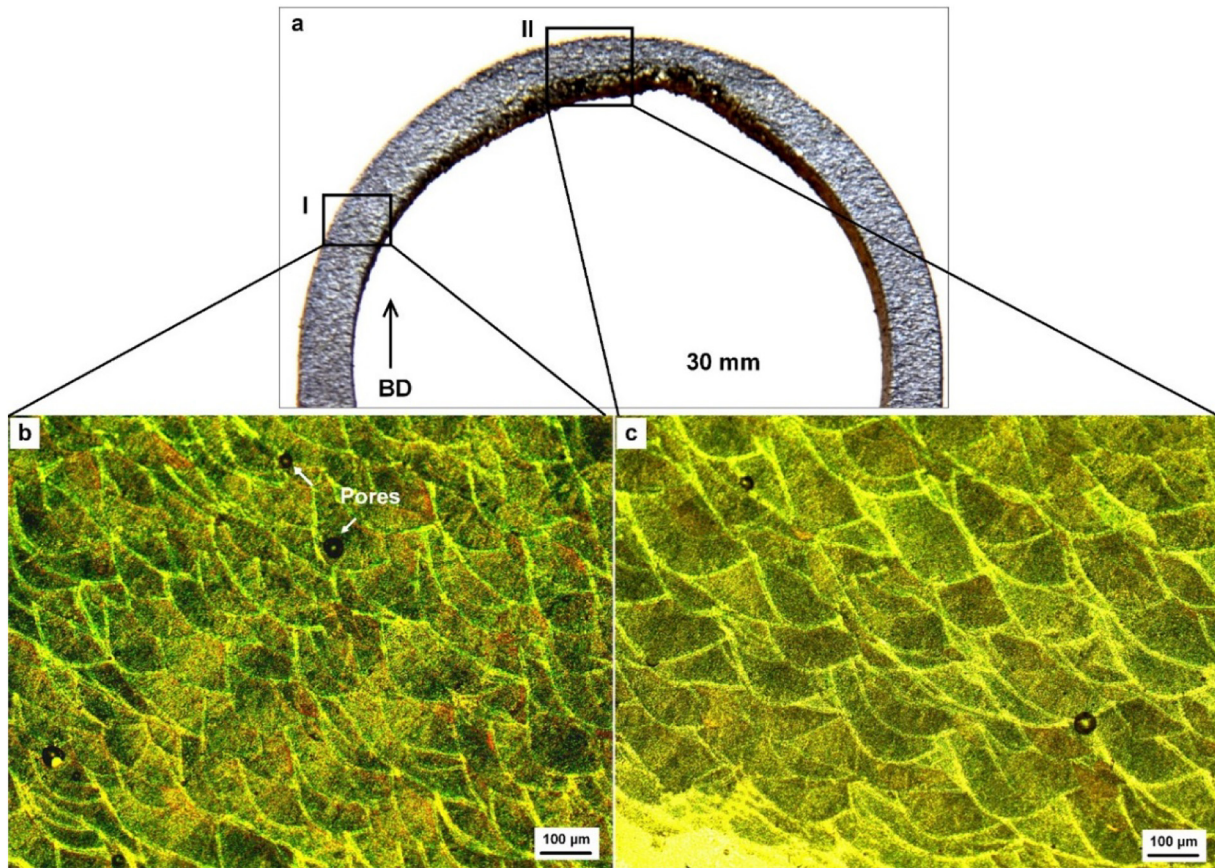
Fig. 11. The molten pool at different positions of the full-circle part-support free (FCPSF) overhang structure.

(Fig. 11a) is shown in Fig. 11b and c, respectively. Because of the layer-by-layer manufacturing principle used in LPBF, the molten pools in region I were fully supported by the underlying solidified layers. In contrast, when part support was not present, position II was only supported by loose powder. The dross was clearly observed in position II due to the lack of solid support. According to the literature, dross defects can be improved by reducing the energy input [14,42]. The microstructure and molten pool size thus should have been different in our study when regions I and II were processed under the same conditions. Indeed, the molten pool in position II was found to be larger than that of region I (Fig. 11b and c). A very limited number of pores were also observed in both regions. The increase in molten pool size from region I to II could be explained by the support structure that was employed. When region I was processed, the molten pool was supported by the underlying solidified layers, which exhibited higher thermal conductivity than the loose powder did. This situation enabled the dissipation of heat energy through the solidified layers, thus accelerating the cooling rate and reducing the size of the molten pools. When region II was processed, loose powder acted as a support and, because of the lower thermal conductivity of loose powder, heat energy accumulated at the laser exposure points and did not dissipate to the surrounding regions. This slower cooling rate favoured the formation of larger molten pools and, together with gravity and surface-tension force in the molten pool, encouraged the formation of the defects we observed.

Fig. 12 shows the molten pool behaviour under bulk support (Fig. 12a) and powder support conditions (Fig. 12b) for the production of a single track. Data from previously published reports [43–46] was used to establish the thermophysical properties of the AlSi10Mg material.

Under the bulk support condition, the generated molten pool size was found to be stable during laser scanning, with a calculated molten pool volume of ~100×10^3 μm^3 (Fig. 12c). The pool size (before the

100 μs mark) could be explained by the loose powder surrounding the molten pool at the start of the track. Fig. 12b/c shows how irregular molten pools were generated when the track was only supported by loose powder, which contributed to the formation of irregularities in the downward-facing surfaces. The calculated average molten pool volume of 450×10^3 μm^3 (Fig. 12c) was much larger than in the previous case. The simulation results confirmed the observation shown in Fig. 11 that larger molten pools were created for downward-facing regions. This finding confirms that the thermal conductivity of supports plays an integral role in the geometric accuracy and structural integrity of LPBF-created metal parts.

Fig. 13 shows the compressive behaviour of the overhang structures under two conditions: WPS and PSF. For the full-circle structures, the overall compressive strength was observed to have increased with a decrease in the nominal diameter from 30 mm to 10 mm under both conditions, while ductility values exhibited the opposite correlation (Fig. 13a). Fracturing was found to have occurred in the middle of the top geometry for all overhang structures (Fig. 13c). The maximum compressive forces for the 30 mm full-circle structure in the PSF and WPS conditions were determined to be 1300 N and 1800 N, respectively. This finding suggests that the part support that was used played a significant role in enhancing the compressive performance: the PSF overhang structures were associated with dross defects, which degraded the mechanical strength.

The maximum compressive forces of the WPS structures were found to have increased from 1800 N to 4000 N, while the PSF structures contributed to a maximum compressive force from 1300 N to 3500 N. The maximum compressive force of the half-circle was found to have increased from 300 N to 1000 N, with a reduction in the nominal diameter from 30 mm to 10 mm (Fig. 13b). Since the fracturing took place at the side geometry in the case of half circle overhang structure, the role of part support was not critical under the compressive load.
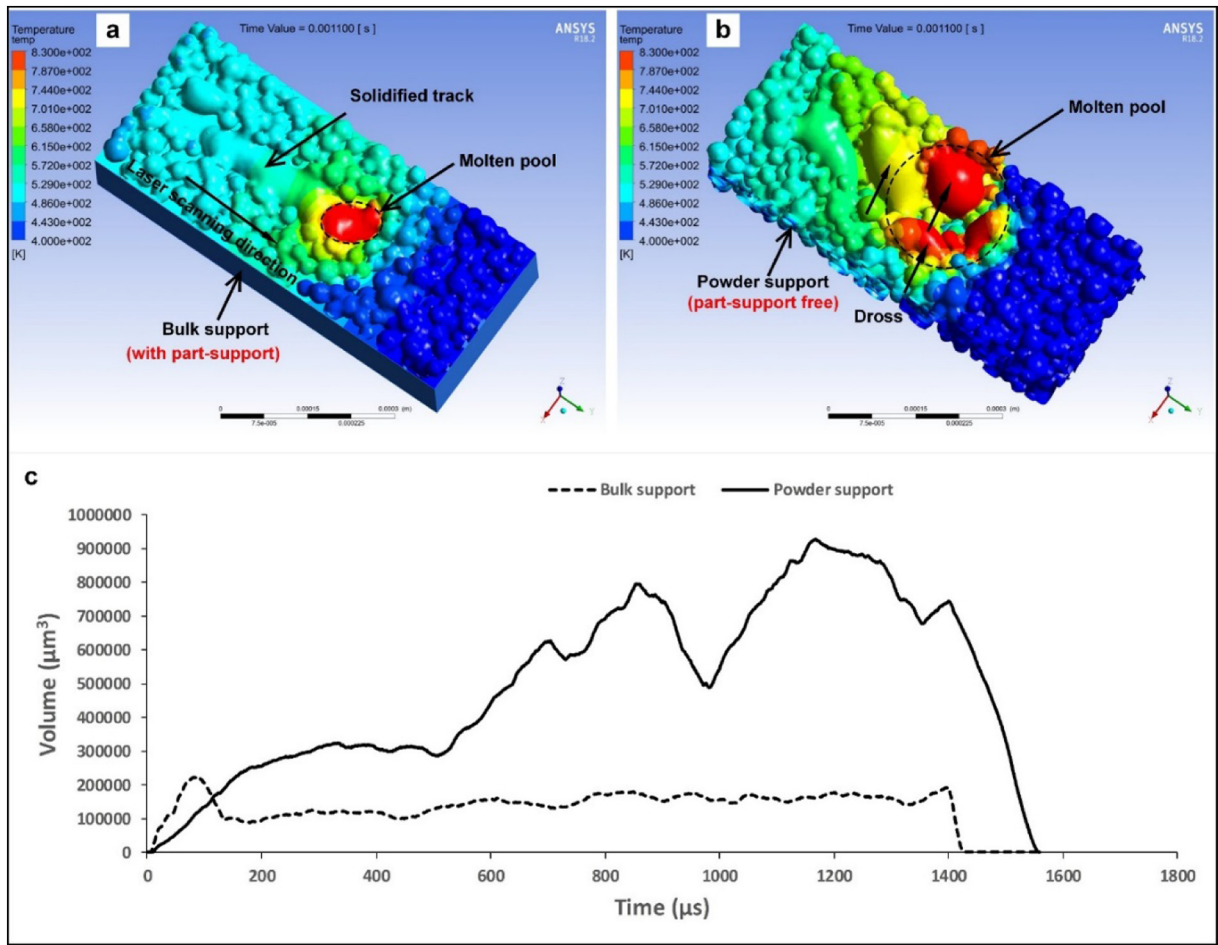
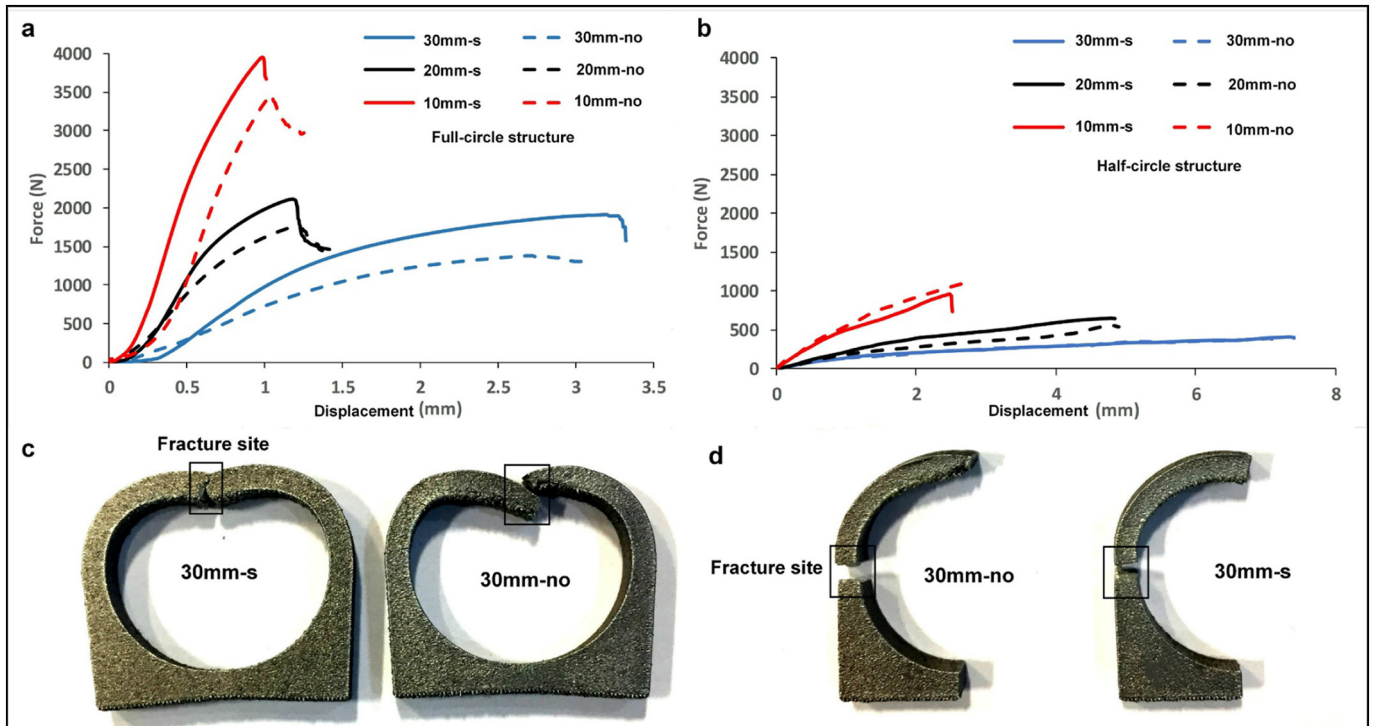**Fig. 12.** The simulated molten pool under two types of support: (a) bulk support; (b) powder support.

Fig. 13. The compressive behaviour of the overhang structures in (a) full-circle structures and (b) half-circle structures; (c–d) photographs of the samples after compression testing. 30 mm-s represents a 30 mm size overhang WPS structure; 30 mm-no represents a 30 mm size overhang structure under the PSF condition.
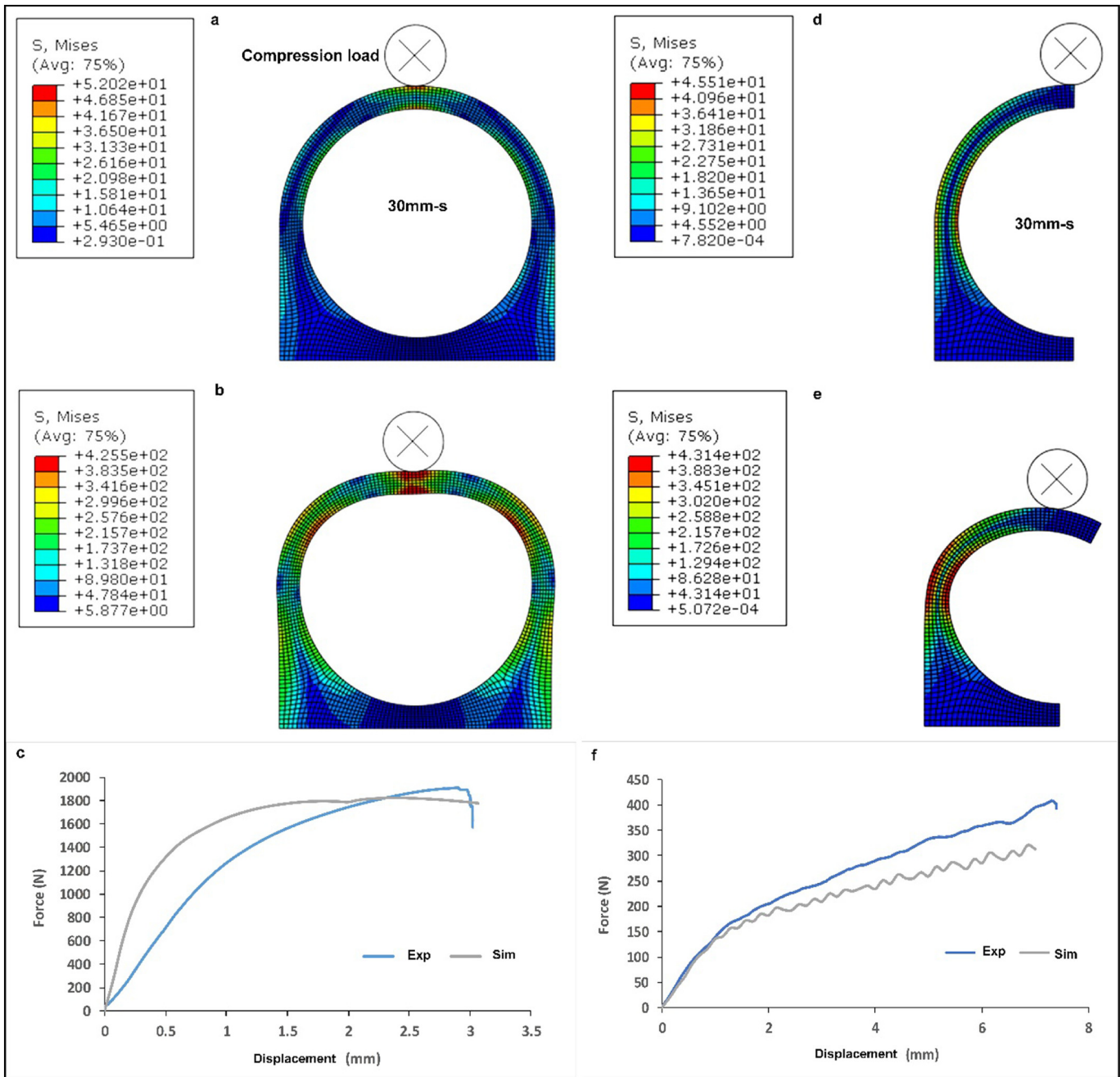
Fig. 14. The simulated compressive behaviour of 30 mm overhang WPS structures: (a–c) full-circle overhang; (d–f) half-circle overhang.

Fig. 14 shows the Abaqus-simulated compressive behaviour of 30 mm overhang structures in the WPS condition. When the full-circle overhang structure was subjected to a compressive load, the initial stress was ~52 MPa, while this value increased to 425.5 MPa at the failure point (Fig. 14a and b). The corresponding compressive forces generated from simulations were also compared with the experimental data (Fig. 14c). The maximum compressive forces were found to be fairly close at the failure point of ~1750 N and ~1900 N for the simulated and experimental conditions, respectively.

It should be noted that the simulation showed a relatively higher compressive response compared to the experiment, but this response converged towards the failure point. This situation could be explained because the LPBF-fabricated overhang structure may have had lower stiffness values compared to the simulation due to the defects (e.g. porosity) and residual stress that were formed within the LPBF process. Compared to the full-circle overhang structure, the half-circle structure was found to exhibit a similar maximum stress value at the failure point, which was determined to be ~431 MPa; the failure site, however, was found to have occurred at the side geometry rather than the top geometry (Fig. 14b and e). In this case, the experiment showed higher compressive strength compared to the simulation at a larger displacement (Fig. 14f); a similar finding was also observed in the smaller circular structures.

Fig. 15 shows the fracture surfaces of the 30 mm full-circle overhang structures under both WPS and PSF conditions. Two distinct regions (I and II) with different microstructures were observed at the fracture surfaces (Fig. 15a and d). The microstructure formed in region I was caused by compression forces in the initial testing phase. This behaviour is similar to how cold working closes open pores and changes the microstructure because of grain and plastic deformation. Delamination was also observed in region I.
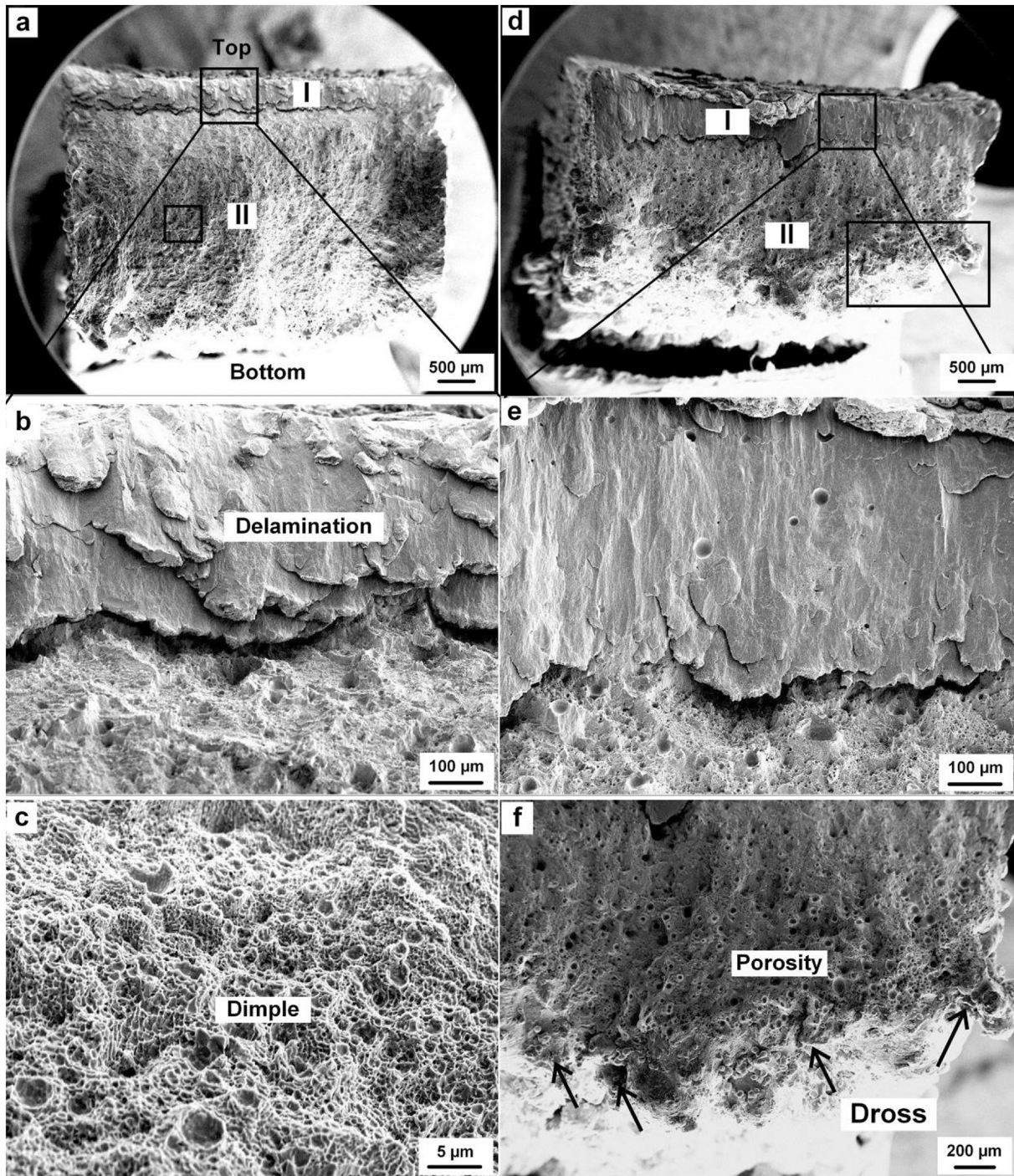
Fig. 15. The fracture surfaces of the 30 mm full-circle overhang structures under (a–c) WPS condition; (d–f) PSF condition.

Region II was subject to tensile loading from the beginning of the compressive testing cycle. The dimple microstructure observed in region II implied a ductile fracture (Fig. 15c). Similar fracture microstructures may also be observed in other tensile-tested aluminium alloys and composites fabricated by LPBF [47,48]. Compared to Fig. 15a–c, Fig. 15d–f depicts a thicker region I and a thinner region II, which is in agreement with the compressive behaviour we observed, where the WPS structure exhibited better compressive performance compared to the PSF structure. Dross defects were also clearly observed in the PSF structure (Fig. 15f), which would degrade the compressive behaviour.

4. Conclusions

This study has investigated the effects of support structures on the manufacturability and structural integrity of AlSi10Mg overhang structures fabricated by laser powder bed fusion (LPBF). The microstructure and compressive behaviour of these structures have also been examined. The following conclusions may be drawn from our experimental and simulation results:

(1) Due to an increase in surface contact area between the built parts and the support structures, the distortion of the LPBF-

manufactured AlSi10Mg overhang structures was significantly reduced compared to those with medium base support.

(2) Part support was found to favour the manufacturability and structural integrity of both full-circle and half-circle overhang structures; the effects were more influential when the nominal diameter increased. The inner circularity value exhibited a linear correlation with the nominal diameter when the nominal diameter was greater than 15 mm, which implies that proper part support is generally needed in order to manufacture dross defect–free overhang structures when the nominal diameter is greater than 15 mm.

(3) The molten pool at the dross zone was found to be both experimentally and theoretically larger than that at the dross-free zone, where the molten pools were supported by the underlying solidified layers. This difference, which is related to the difference in thermal conductivity between bulk solidified layers and loose powder.

(4) During compressive testing, part support was found to play a more important role in enhancing the compressive behaviour of full-circle overhang structures than of half-circle structures.

(5) The application of several computational methods, including Simufact Additive, ANSYS Fluent and Abaqus, was vital in understanding both process and structural performance. These findings will likely lead to the further development of self-supporting structures in future studies.

These results demonstrate the influence of support structures on the manufacturability and mechanical properties of AlSi10Mg overhang structures produced by LPBF. The selection of suitable support structures should be carefully taken into consideration when building metal LPBF parts in order to guarantee structural integrity and geometrical accuracy while at the same time limiting the post-processing operation involved in these structures' removal.

Acknowledgements

References

[1] G. Strano, L. Hao, R.M. Everson, K.E. Evans, Surface roughness analysis, modelling and prediction in selective laser melting, J. Mater. Process. Technol. (4) (2013) 589–597, https://doi.org/10.1016/j.jmatprotec.2012.11.011.
[2] Q. Han, Y. Geng, R. Setchi, F. Lacan, D. Gu, S.L. Evans, Macro and nanoscale wear behaviour of Al-Al₂O₃ nanocomposites fabricated by selective laser melting, Compos. Part B Eng. 127 (2017) 26–35, https://doi.org/10.1016/j.compositesb.2017.06.026.
[3] N.T. Aboulkhair, I. Maskery, C. Tuck, I. Ashcroft, N.M. Everitt, Improving the fatigue behaviour of a selectively laser melted aluminium alloy: influence of heat treatment and surface quality, Mater. Des. 104 (2016) 174–182, https://doi.org/10.1016/j.matdes.2016.05.041.
[4] Q. Han, R. Setchi, S.L. Evans, Characterisation and milling time optimisation of nanocrystalline aluminium powder for selective laser melting, Int. J. Adv. Manuf. Technol. 88 (2017) 1429–1438, https://doi.org/10.1007/s00170-016-8866-z.
[5] Q. Han, R. Setchi, S.L. Evans, Synthesis and characterisation of advanced ball-milled Al-Al₂O₃ nanocomposites for selective laser melting, Powder Technol. 297 (2016) 183–192, https://doi.org/10.1016/j.powtec.2016.04.015.
[6] H. Attar, S. Ehtemam-Haghighi, D. Kent, X. Wu, M.S. Dargusch, Comparative study of commercially pure titanium produced by laser engineered net shaping, selective laser melting and casting processes, Mater. Sci. Eng. A 705 (2017) 385–393, https://doi.org/10.1016/j.msea.2017.08.103.
[7] A. Sarker, N. Tran, A. Rifai, J. Elambasseril, M. Brandt, R. Williams, M. Leary, K. Fox, Angle defines attachment: switching the biological response to titanium interfaces by modifying the inclination angle during selective laser melting, Mater. Des. 154 (2018) 326–339, https://doi.org/10.1016/j.matdes.2018.05.043.
[8] Z. Xu, C.J. Hyde, A. Thompson, R.K. Leach, I. Maskery, C. Tuck, A.T. Clare, Staged thermomechanical testing of nickel superalloys produced by selective laser melting, Mater. Des. 133 (2017) 520–527, https://doi.org/10.1016/j.matdes.2017.08.009.
[9] S. Catchpole-Smith, N. Aboulkhair, L. Parry, C. Tuck, I.A. Ashcroft, A. Clare, Fractal scan strategies for selective laser melting of 'unweldable' nickel superalloys, Addit. Manuf. 15 (2017) 113–122, https://doi.org/10.1016/j.addma.2017.02.002.
[10] Q. Han, R. Mertens, M. Montero-Sistiaga, S. Yang, R. Setchi, K. Vanmeensel, B. Hooreweder, S.L. Evans, H. Fan, Laser powder bed fusion of Hastelloy X: effects of hot isostatic pressing and the hot cracking mechanism, Mater. Sci. Eng. A 732 (2018) 228–239, https://doi.org/10.1016/j.msea.2018.07.008.
[11] Y.J. Liu, X.P. Li, L.C. Zhang, T.B. Sercombe, Processing and properties of topologically optimised biomedical Ti-24Nb-4Zr-8Sn scaffolds manufactured by selective laser melting, Mater. Sci. Eng. A 642 (2015) 268–278, https://doi.org/10.1016/j.msea.2015.06.088.
[12] S. Li, H. Hassanin, M.M. Attallah, N.J.E. Adkins, K. Essa, The development of TiNi-based negative Poisson's ratio structure using selective laser melting, Acta Mater. 105 (2016) 75–83, https://doi.org/10.1016/j.actamat.2015.12.017.
[13] M. Leary, M. Mazur, J. Elambasseril, M. McMillan, T. Chirent, Y. Sun, M. Qian, M. Easton, M. Brandt, Selective laser melting (SLM) of AlSi12Mg lattice structures, Mater. Des. 98 (2016) 344–357, https://doi.org/10.1016/j.matdes.2016.02.127.
[14] D. Wang, S. Mai, D. Xiao, Y. Yang, Surface quality of the curved overhanging structure manufactured from 316-L stainless steel by SLM, Int. J. Adv. Manuf. Technol. 86 (2016) 781–792, https://doi.org/10.1007/s00170-015-8216-6.
[15] F. Calignano, Design optimization of supports for overhanging structures in aluminum and titanium alloys by selective laser melting, Mater. Des. 64 (2014) 203–213, https://doi.org/10.1016/j.matdes.2014.07.043.
[16] I. Yadroitsev, I. Shishkovsky, P. Bertrand, I. Smurov, Manufacturing of fine-structured 3D porous filter elements by selective laser melting, Appl. Surf. Sci. 255 (2009) 5523–5527, https://doi.org/10.1016/j.apsusc.2008.07.154.
[17] F. Calignano, D. Manfredi, E.P. Ambrosio, L. Iuliano, P. Fino, Influence of process parameters on surface roughness of aluminum parts produced by DMLS, Int. J. Adv. Manuf. Technol. 67 (2013) 2743–2751, https://doi.org/10.1007/s00170-012-4688-9.
[18] K. Cooper, P. Steele, B. Cheng, K. Chou, Contact-free support structures for part overhangs in powder-bed metal additive manufacturing, Inventions 3 (2017) 2, https://doi.org/10.3390/inventions3010002.
[19] G. Strano, L. Hao, R.M. Everson, K.E. Evans, A new approach to the design and optimisation of support structures in additive manufacturing, Int. J. Adv. Manuf. Technol. 66 (2013) 1247–1254, https://doi.org/10.1007/s00170-012-4403-x.
[20] M. Langelaar, Combined optimization of part topology, support structure layout and build orientation for additive manufacturing, Struct. Multidiscip. Optim. 57 (2018) 1985–2004, https://doi.org/10.1007/s00158-017-1877-z.
[21] F. Mezzadri, V. Bouriakov, X. Qian, Topology optimization of self-supporting support structures for additive manufacturing, Addit. Manuf. 21 (2018) 666–682, https://doi.org/10.1016/j.addma.2018.04.016.
[22] Y. Kajima, A. Takaichi, T. Nakamoto, T. Kimura, N. Kittikundecha, Y. Tsutsumi, N. Nomura, A. Kawasaki, H. Takahashi, T. Hanawa, N. Wakabayashi, Effect of adding support structures for overhanging part on fatigue strength in selective laser melting, J. Mech. Behav. Biomed. Mater. 78 (2018) 1–9, https://doi.org/10.1016/j.jmbbm.2017.11.009.
[23] X. Wang, K. Chou, Effect of support structures on Ti-6Al-4V overhang parts fabricated by powder bed fusion electron beam additive manufacturing, J. Mater. Process. Technol. 257 (2018) 65–78, https://doi.org/10.1016/j.jmatprotec.2018.02.038.
[24] S.L. Sing, F.E. Wiria, W.Y. Yeong, Selective laser melting of lattice structures: a statistical approach to manufacturability and mechanical behavior, Robot. Comput. Integr. Manuf. 49 (2018) 170–180, https://doi.org/10.1016/j.rcim.2017.06.006.
[25] F. Calignano, Investigation of the accuracy and roughness in the laser powder bed fusion process, Vis. Phys. Prototyp. 13 (2018) 97–104.
[26] J.A. Collins, Mechanical Design of Machine Elements and Machines: A Failure Prevention Perspective, John Wiley & Sons, 2010 https://doi.org/10.1115/1.1635406.
[27] C. Yan, L. Hao, A. Hussein, P. Young, D. Raymont, Advanced lightweight 316L stainless steel cellular lattice structures fabricated via selective laser melting, Mater. Des. 55 (2014) 533–541, https://doi.org/10.1016/j.matdes.2013.10.027.
[28] H. Brooks, K. Brigden, Design of conformal cooling layers with self-supporting lattices for additively manufactured tooling, Addit. Manuf. 11 (2016) 16–22, https://doi.org/10.1016/j.addma.2016.03.004.
[29] J.A. Harris, R.E. Winter, G.J. McShane, Impact response of additively manufactured metallic hybrid lattice materials, Int. J. Impact Eng. 104 (2017) 177–191, https://doi.org/10.1016/j.ijimpeng.2017.02.007.
[30] Y. Wang, L. Zhang, S. Daynes, H. Zhang, S. Feih, M.Y. Wang, Design of graded lattice structure with optimized mesostructures for additive manufacturing, Mater. Des. 142 (2018) 114–123, https://doi.org/10.1016/j.matdes.2018.01.011.
[31] I. Setien, M. Chiumenti, S. van der Veen, M. San Sebastian, F. Garciandía, A. Echeverría, Empirical methodology to determine inherent strains in additive manufacturing, Comput. Math. Appl. (2018) https://doi.org/10.1016/j.camwa.2018.05.015.
[32] N, https://www.simufact.com/simufact-additive.html, Accessed date: 3 September 2018 (n.d.).
[33] G.K. Batchelor, An Introduction to Fluid Dynamics, Book, 1967 https://doi.org/10.1063/1.3060769.
[34] V.R. Voller, C. Prakash, A fixed grid numerical modelling methodology for convection-diffusion mushy region phase-change problems, Int. J. Heat Mass Transf. 30 (1987) 1709–1719, https://doi.org/10.1016/0017-9310(87)90317-6.
[35] V.R. Voller, A.D. Brent, C. Prakash, The modelling of heat, mass and solute transport in solidification systems, Int. J. Heat Mass Transf. 32 (1989) 1719–1731, https://doi.org/10.1016/0017-9310(89)90054-9.
[36] C.W. Hirt, B.D. Nichols, Volume of fluid (VOF) method for the dynamics of free boundaries, J. Comput. Phys. 39 (1981) 201–225, https://doi.org/10.1016/0021-9991(81)90145-5.

[37] M.H. Cho, Y.C. Lim, D.F. Farson, Simulation of weld pool dynamics in the stationary pulsed gas metal arc welding process and final weld shape, Weld. J. 85 (2006) 271.

[38] J.I. Arrizubieta, A. Lamikiz, F. Klocke, S. Martínez, K. Arntz, E. Ukar, Evaluation of the relevance of melt pool dynamics in laser material deposition process modeling, Int. J. Heat Mass Transf. 115 ((2017) 80–91, https://doi.org/10.1016/j.ijheatmasstransfer.2017.07.011.

[39] Data sheets-additive manufacturing, http://www.renishaw.com/en/data-sheets-additive-manufacturing–17862, Accessed date: 4 August 2018 (n.d.).

[40] B. Vandenbroucke, J.P. Kruth, Selective laser melting of biocompatible metals for rapid manufacturing of medical parts, Rapid Prototyp. J. 13 (2007) 196–203, https://doi.org/10.1108/13552540710776142.

[41] O. Rehme, C. Emmelmann, Rapid manufacturing of lattice structures with selective laser melting, Laser-Based Micropackag. 6107 (2006)https://doi.org/10.1117/12.645848 (61070K–61070K–12).

[42] H. Chen, D. Gu, J. Xiong, M. Xia, Improving additive manufacturing processability of hard-to-process overhanging structure by selective laser melting, J. Mater. Process. Technol. 250 (2017) 99–108, https://doi.org/10.1016/j.jmatprotec.2017.06.044.

[43] P. Yuan, D. Gu, Molten pool behaviour and its physical mechanism during selective laser melting of TiC/AlSi10Mg nanocomposites: simulation and experiments, J. Phys. D. Appl. Phys. 48 (2015), 035303. https://doi.org/10.1088/0022-3727/48/3/035303.

[44] J. Nandy, H. Sarangi, S. Sahoo, Modeling of microstructure evolution in direct metal laser sintering: a phase field approach, IOP Conf. Ser. Mater. Sci. Eng. 178 (2017), 012028. https://doi.org/10.1088/1757-899X/178/1/012028.

[45] L. Dou, Z.F. Yuan, J.Q. Li, J. Li, X.Q. Wang, Surface tension of molten Al-Si alloy at temperatures ranging from 923 to 1123 K, Chin. Sci. Bull. 53 (2008) 2593–2598, https://doi.org/10.1007/s11434-008-0372-8.

[46] A. Ojha, M. Samantaray, D. Nath Thatoi, S. Sahoo, Continuum simulation of heat transfer and solidification behavior of AlSi10Mg in direct metal laser sintering process, IOP Conf. Ser. Mater. Sci. Eng. 338 (2018) 012052, https://doi.org/10.1088/1757-899X/338/1/012052.

[47] N. Read, W. Wang, K. Essa, M.M. Attallah, Selective laser melting of AlSi10Mg alloy: process optimisation and mechanical properties development, Mater. Des. 65 (2015) 417–424, https://doi.org/10.1016/j.matdes.2014.09.044.

[48] Q. Han, R. Setchi, F. Lacan, D. Gu, S.L. Evans, Selective laser melting of advanced Al-Al$_2$O$_3$ nanocomposites: simulation, microstructure and mechanical properties, Mater. Sci. Eng. A 698 (2017) 162–173, https://doi.org/10.1016/j.msea.2017.05.061.